

X-ray binaries with neutron stars at different accretion stages

Konstantin A. Postnov^{1,2}, Alexander G. Kuranov^{1,3} & Lev R. Yungelson⁴

¹Sternberg Astronomical Institute, Moscow M.V. Lomonosov State University
 13 Universitetskij pr., 119234 Moscow, Russia
 email: pk@sai.msu.ru

²Kazan Federal University, 18 Kremlyovskaya str., 420008 Kazan, Russia

³Russian Foreign Trade Academy, 4 Pudovkin str., 119285 Moscow, Russia

⁴Institute of Astronomy, RAS, 48 Pyatnitskaya str., 119017 Moscow, Russia
 email: lry@inasan.ru

Abstract. Different accretion regimes onto magnetized NSs in HMXBs are considered: wind-fed supersonic (Bondi) regime at high accretion rates $\dot{M} \gtrsim 4 \times 10^{16} \text{ [g s}^{-1}\text{]}$, subsonic settling regime at lower \dot{M} and supercritical disc accretion during Roche lobe overflow. In wind-fed stage, NSs in HMXBs reach equilibrium spin periods P^* proportional to binary orbital period P_b . At supercritical accretion stage, the system may appear as a pulsating ULX. Population synthesis of Galactic HMXBs using standard assumptions on the binary evolution and NS formation is presented. Comparison of the model $P^* - P_b$ (the Corbet diagram), $P^* - L_x$ and $P_b - L_x$ distributions with those for the observed HMXBs (including Be X-ray binaries) and pulsating ULXs suggests the importance of the reduction of P^* in non-circular orbits, explaining the location of Be X-ray binaries in the model Corbet diagram, and the universal parameters of pulsating ULXs depending only on the NS magnetic fields.

Keywords. accretion, accretion disks; binaries: close; stars: neutron

1. Introduction

High-mass X-ray binaries (HMXBs) are important tools to study binary evolution (see other papers in this volume). Here we focus on two particular aspects of accretion onto magnetized neutron stars (NSs) in HMXBs that have important observational manifestations: wind accretion in the settling (subsonic regime), which is relevant at moderate and low accretion rates onto NS, $\dot{M} \lesssim 4 \times 10^{16} \text{ [g s}^{-1}\text{]}$. For wind accretion in HMXBs with $\dot{M} > 4 \times 10^{16} \text{ [g s}^{-1}\text{]}$, the supersonic Bondi-Hoyle-Littleton accretion takes place. We separately consider HMXBs with supercritical disc accretion at $\dot{M} \gtrsim 10^{18} \text{ [g s}^{-1}\text{]}$, which is relevant to the growing class of pulsating ultraluminous X-ray sources (ULXs) (see F. Harrison and F. Fürst papers in this volume).

2. Settling wind accretion in HMXBs: an overview

The settling accretion theory is designed to describe the interaction of accreting plasma with magnetospheres of slowly rotating NSs (see Shakura et al. (2018) for a detailed derivation and discussion). The key feature of the model is the calculation of the plasma entry rate into the magnetosphere due to the Rayleigh-Taylor (RT) instability regulated by plasma cooling (Compton or radiative). RT instability can be suppressed by the fast rotation of the magnetosphere (Arons & Lea 1980), and settling accretion regime can

be realized for NS spin periods $P^* > 27[s] \dot{M}_{16}^{1/5} \mu_{30}^{33/35} (M_x/M_\odot)^{-97/70}$. At shorter NS periods, accretion regime at any X-ray luminosity will be supersonic because of efficient plasma penetration into the magnetosphere via Kelvin-Helmholtz instability (Burnard et al. 1983). Here and below, accretion rate $\dot{M} = \dot{M}_{16} \times 10^{16} [\text{g s}^{-1}]$, NS magnetic moment $\mu = \mu_{30} \times 10^{30} [\text{G cm}^3]$. Compton cooling of accreting plasma by X-ray photons generated near the NS surface enables a free-fall (Bondi-type) supersonic accretion onto the NS magnetosphere provided that the X-ray luminosity is above the critical value $L_x^\dagger \simeq 4 \times 10^{36} \text{ erg s}^{-1}$ (Shakura et al. 2012), corresponding to the mass accretion rate onto NS $\dot{M}_x \simeq 4 \times 10^{16} [\text{g s}^{-1}]$. At lower X-ray luminosities, the plasma above the magnetosphere remains hot enough to avoid an effective inflow into the magnetosphere due to RT instability, and the plasma entry rate is controlled by the cooling rate. This results in the formation of a hot, convective shell above the magnetosphere. In this shell, the plasma gravitationally captured by the neutron star from the stellar wind of the companion (basically, at the Bondi-Hoyle-Littleton rate, \dot{M}_B) settles towards the NS magnetosphere at a rate $\dot{M}_x = f(u)\dot{M}_B$, with the dimensionless factor $f(u) \lesssim 0.5^\dagger$, whose precise value depends on the plasma cooling regime (Compton or radiative). With a good accuracy, this factor can be written as $f(u) \approx (t_{\text{ff}}/t_{\text{cool}})^{1/3}$, where t_{ff} is the free-fall time at the magnetospheric boundary (the Alfvén radius, R_A), t_{cool} is the characteristic plasma cooling time. Clearly, in the case $t_{\text{cool}} \gg t_{\text{ff}}$, this factor can be very small, leading to an effective decrease in the mass accretion rate onto the NS surface compared to the maximum possible Bondi rate, \dot{M}_B .

In a circular binary system with the components separation a , Bondi-Hoyle-Littleton accretion rate can be estimated as

$$\dot{M}_B \approx \frac{1}{4} \dot{M}_o \frac{v}{v_w} \left(\frac{R_B}{a} \right)^2, \quad (2.1)$$

where \dot{M}_o is the optical star wind mass-loss rate, gravitational Bondi radius $R_B = \delta \frac{2GM_x}{v^2}$, M_x – NS mass, $v^2 = v_{\text{orb},x}^2 + v_w^2$ – relative stellar wind velocity, $v_{\text{orb},x}$ – NS orbital velocity. The estimate (2.1) assumes a spherically-symmetric wind from the optical star and is applicable for $R_B \ll a$. Numerical factor $\delta \sim 1$ takes into account the actual location of the bow shock in the stellar wind (Hunt 1971). Modern numerical calculations (see, e.g., Liu et al. 2017) suggest smaller (up to an order of magnitude) mass accretion rates onto a gravitating mass from the stellar wind than given by the standard Bondi-Hoyle-Littleton formula, which can be reformulated in terms of smaller values of the parameter $\delta \simeq 0.3 - 0.5$. Other studies (e.g., de Val-Borro et al. 2017) claim that accretion rate can exceed the Bondi one due to focusing of the wind. Therefore, the numerical factor δ can differ from unity by a factor of a few.

The Alfvén radius is defined from the pressure balance between the accreting plasma and the magnetic field at the magnetospheric boundary and depends on the actual mass accretion rate, \dot{M}_x (i.e., the observable X-ray luminosity L_x), and the neutron star magnetic moment, μ : $R_A \sim (f(u)\mu^2/(\dot{M}_x\sqrt{GM_x}))^{2/7}$. Factor $f(u)$ is

$$f(u)_{\text{Comp}} \approx 0.22 \zeta^{7/11} \dot{M}_{x,16}^{4/11} \mu_{30}^{-1/11} \quad (2.2)$$

and

$$f(u)_{\text{rad}} \approx 0.1 \zeta^{14/81} \dot{M}_{x,16}^{6/27} \mu_{30}^{2/27} \quad (2.3)$$

[†] In a radial accretion flow with an account of the Compton cooling, the value $f(u) \gtrsim 0.5$ also corresponds to the location of the sonic point below the magnetospheric boundary R_A (Shakura et al. 2012) enabling a free-fall plasma flow down to R_A and the formation of a shock above the magnetosphere (Arons & Lea 1976).

for the Compton and radiative cooling, respectively (Shakura & Postnov 2017; Shakura et al. 2018). Here $\zeta \lesssim 1$ is the numerical factor determining the characteristic scale of the growing RT mode (in the units of the Alfvén radius R_A).

Thus, specifying the plasma cooling mechanism, we are able to estimate the expected reduction in the mass accretion rate at the settling accretion stage, $f(u) = F(\dot{M}_x, \dots) = F(f(u)\dot{M}_B, \dots)$, and by solving for $f(u)$, to find the explicit expression for \dot{M}_x as a function of \dot{M}_B and other parameters.

Putting all things together, we are able to express the expected accretion rate onto the NS (which can be directly probed by the observed X-ray luminosity L_x) using the Bondi capture rate \dot{M}_B , which can be calculated from the known mass-loss rate of the optical companion \dot{M}_o , stellar wind velocity v_w and binary system parameters:

$$\dot{M}_{x,16}^{\text{Comp}} \simeq 0.1\zeta \dot{M}_{B,16}^{11/7} \mu_{30}^{-1/7} \quad (2.4)$$

for the Compton cooling and

$$\dot{M}_{x,16}^{\text{rad}} \simeq 0.05\zeta^{2/9} \dot{M}_{B,16}^{9/7} \mu_{30}^{2/21} \quad (2.5)$$

for the radiative cooling. The actual accretion rate onto NS is taken to be $\dot{M}_x = \max\{\dot{M}_x^{\text{Comp}}, \dot{M}_x^{\text{rad}}\}$ and determines the cooling regime. Matching Eq. (2.4) and Eq. (2.5) shows that for a given NS magnetic momentum, the Compton cooling of plasma dominates for the gravitational capture mass rate $\dot{M}_{B,16} \gtrsim 0.1\zeta^{-2/9} \mu_{30}^{5/6}$.

During the settling accretion stage, a hot convective shell formed above the NS magnetosphere mediates the angular momentum transfer to/from the rotating NS enabling long-term spin-down episodes with spin-down torques correlated with the X-ray luminosity, as observed, for example, in GX 1+4 (Chakrabarty et al. 1997; González-Galán et al. 2012). Turbulent stresses acting in the shell lead to an almost iso-momentum angular velocity radial distribution, $\omega(r) \sim 1/r^2$, suggesting the conservation of the specific angular momentum of gas captured near the Bondi radius R_B , $j_w = \eta\omega_b R_B^2$, $\eta \approx 1/4$ (Illarionov & Sunyaev 1975), where $\omega_b = 2\pi/P_b$ is the orbital angular frequency. The numerical coefficient η here can vary in a wide range due to inhomogeneities in the stellar wind and can be even negative (Ho et al. 1989) leading to a temporal formation of retrograde accretion discs. In our calculations, we varied this parameter in the range $\eta = [0, 0.25]$.

The condition for a quasi-spherical accretion to occur is that the specific angular momentum of a gas parcel is smaller than the Keplerian angular momentum at the Alfvén radius: $j_w \leq j_K(R_A) = \sqrt{GM_x R_A}$. In the opposite case, $j_w > j_K(R_A)$, the formation of an accretion disc around the magnetosphere is possible.

The equation for spin evolution of a NS at the settling accretion stage can be written in the form (Shakura et al. 2012, 2018)

$$\frac{dI\omega^*}{dt} = \eta Z \dot{M}_x \omega_b R_B^2 - Z(1 - z/Z) \dot{M}_x \omega^* R_A^2, \quad (2.6)$$

where I is the NS momentum of inertia, the coupling coefficient of the plasma-magnetosphere interaction is $Z = 1/f(u)(u_c/u_{ff})$, $u_c/u_{ff} \lesssim 1$ is the ratio of the convective velocity in the shell and the free-fall velocity, $z \lesssim 1$ is a numerical coefficient which takes into account the angular momentum of the falling matter at the NS surface. The account of the variable specific angular momentum of the gravitationally captured stellar wind leads to the correction of the equilibrium NS period derived in Shakura et al. (2012, 2018) by the factor $0.25/\eta$. In the possible case of a negative value of η , NS would rapidly spin-down and even start to temporarily rotate in the retrograde direction. However, it is difficult to imagine that such a situation holds much longer than the orbital binary

period. Therefore, the possible episodes with negative η would somewhat increase the NS equilibrium period P_{eq} which we recalculate at each time step of our population synthesis calculations. Therefore, we will consider only positive values of η and restrict the NS spin rotation by the orbital binary periods, $P^* \leq P_b$.

Orbital eccentricity effect.

Here we describe the effect of orbital eccentricity e on the value of the equilibrium NS period at the settling accretion stage. Because of the orbital eccentricity, the spin-up and spin-down torques applied to NS change and should be averaged over the orbital period. In the standard Keplerian problem, the separation between barycenters of the binary components $r = p/(1 + e \cos \theta)$, where $p = a(1 - e^2)$ – orbital semilatus rectum, a – large semi-major axis of the orbit, e – orbital eccentricity, θ – true anomaly. Stellar wind is assumed to be spherically symmetric and centered at the optical star barycenter. The radius of the optical star is R_o , and the stellar wind velocity as a function of distance from the star is normalized to the parabolic velocity at the optical star photosphere, $v_{esc} = \sqrt{2GM_o/R_o}$. It can be written as $v_w(r) = v_{esc}f(r)$. For example, for the radiative-driven accelerating winds from early type stars $f(r) = \alpha(1 - R_o/r)^\beta$ where $\alpha = 0.7...3.8$ and $\beta = 0.7...2.0$ are obtained from recent numerical simulations (Vink 2018).

In the case of a non-circular orbit, specific angular momentum of captured wind matter is determined by the normal component of the NS orbital velocity and changes along the orbit: $j(\theta) \sim v_n(\theta)R_B(\theta)[R_B(\theta)/r(\theta)]$ (here $v_n = \sqrt{GM/p(1 + e \cos \theta)}$, $M = M_o + M_x$), while the gravitational capture Bondi radius $R_B(\theta)$ depends on the module of the sum of the orbital velocity vector \mathbf{v}_{orb} and the wind velocity vector \mathbf{v}_w : $R_B(\theta) \sim 2GM_x/v(\theta)^2$, where $v(\theta) = \sqrt{[v_w(r(\theta)) - v_r(\theta)]^2 + v_n^2(\theta)}$ (here the radial component of the orbital velocity is $v_r(\theta) = v_n = \sqrt{GM/p(1 + e \cos \theta)}$).

Thus, by averaging the spin-up/spin-down Eq. (2.6) over orbit $r(\theta)$, we find NS equilibrium period:

$$\overline{P_{eq}} = 2\pi \frac{\langle \dot{M}_B R_A^2 \rangle}{\langle \dot{M}_B v_n R_B(R_B/r) \rangle}. \quad (2.7)$$

The orbit-averaged value $\overline{P_{eq}}$ can be written using the equilibrium period calculated for a circular orbit, $P_{eq} \approx P_b(R_A/R_B)^2$, as $\overline{P_{eq}} = F(e)P_{eq}$, where the factor $F(e) < 1$ is plotted in Fig. 1. A significant decrease of the equilibrium NSs periods may occur for highly eccentric binaries (e.g., Be X-ray binaries, BeXBs). Indeed, they are located below HMXBs with almost circular orbits in the Corbet diagram. Thus, the eccentricity effect can explain the observed diversity of X-ray pulsar populations in HMXBs produced by different types of supernova noted by Knigge et al. (2011).

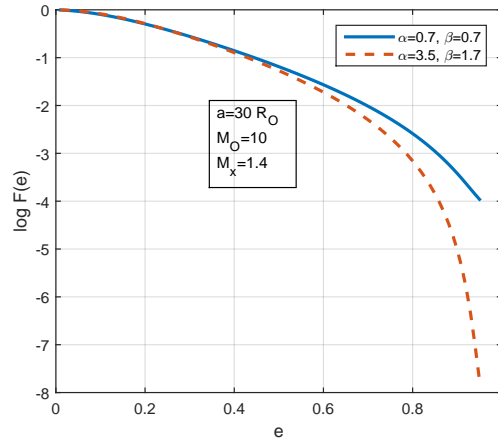


Figure 1. Reduction factor $F(e)$ for the equilibrium NSs periods at the settling accretion stage in the non-circular orbits for the range of radiative stellar wind parameters α and β .

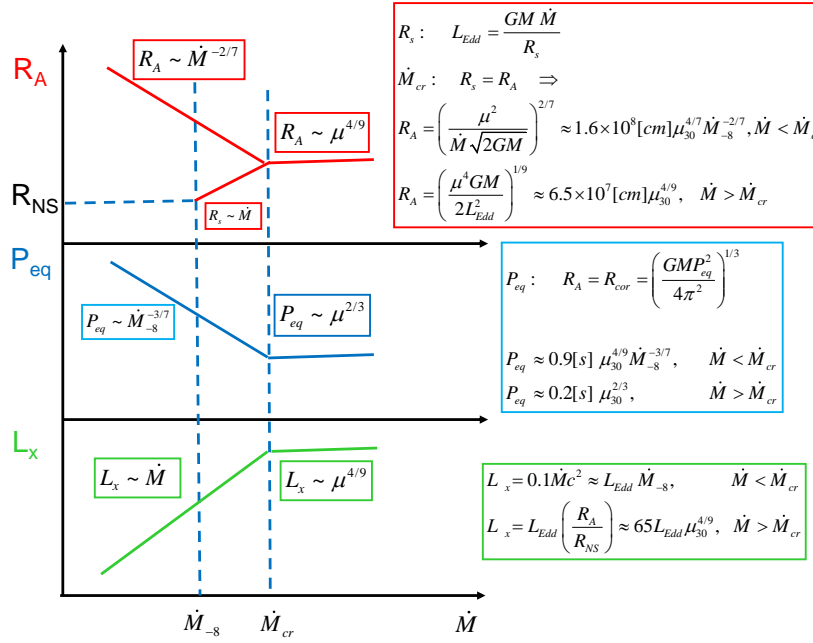


Figure 2. The Alfvén radius (top), equilibrium NS period (middle) and X-ray luminosity (bottom) for supercritical accretion discs around magnetized NSs (see the text).

3. Supercritical accretion onto magnetized NSs

In HMXBs with Roche overflow by the optical star, a supercritical disc accretion regime must occur (Shakura & Sunyaev 1973). In this regime, a radiation-driven outflow occurs in the disc starting from the spherization radius $R_s = GM_x \dot{M} / L_{Edd}$, where $L_{Edd} \simeq 10^{38} (M_x / M_\odot) [\text{erg s}^{-1}]$ is the Eddington luminosity corresponding to $\dot{M}_{Edd} \simeq 10^{18} [\text{g s}^{-1}]$. A feature of the supercritical accretion onto a magnetized NS is the appearance of a critical luminosity (mass accretion rate) at which the Alfvén radius R_A becomes comparable to the spherization radius R_s as shown in the scheme in Fig. 2 (see also Lipunov (1982); King et al. (2017)), $\dot{M}_{cr} \simeq 3 \times 10^{19} \mu_{30}^{4/9} [\text{g s}^{-1}]$. As long as mass accretion rate in the supercritical disc increases and $\dot{M}_{Edd} < \dot{M} < \dot{M}_{cr}$, NS magnetospheric radius decreases, $R_A \sim \dot{M}^{-2/7}$, its equilibrium period decreases, $P^* \sim \dot{M}^{-5/7}$, and the X-ray luminosity generated at the NS surface increases, $L_x \sim \dot{M}$. After reaching \dot{M}_{cr} , NS magnetosphere stops to decrease because of the wind outflow from $R_s = R_A$ (see Fig. 2), and for $\dot{M} > \dot{M}_{cr}$ all three quantities, R_A , P_{eq} and L_x become dependent on the NS magnetic field only (the latter to within a logarithmic correction $1 + \ln(\dot{M} / \dot{M}_{Edd})$, Shakura & Sunyaev (1973)).

4. Population synthesis of HMXBs

We use a modified version of the openly available BSE code (Hurley et al. 2000, 2002) appended by the block for calculation of spin evolution of magnetized neutron stars (Lipunov et al. 2009) with account for settling accretion regime (see also Lü et al. 2012, for more detail). The standard HMXB evolutionary scenario is used (Postnov & Yungelson 2014). We have used the convolution of the HMXB formation rate after instantaneous star-formation burst with Galactic star-formation rate in the Galactic bulge and thin

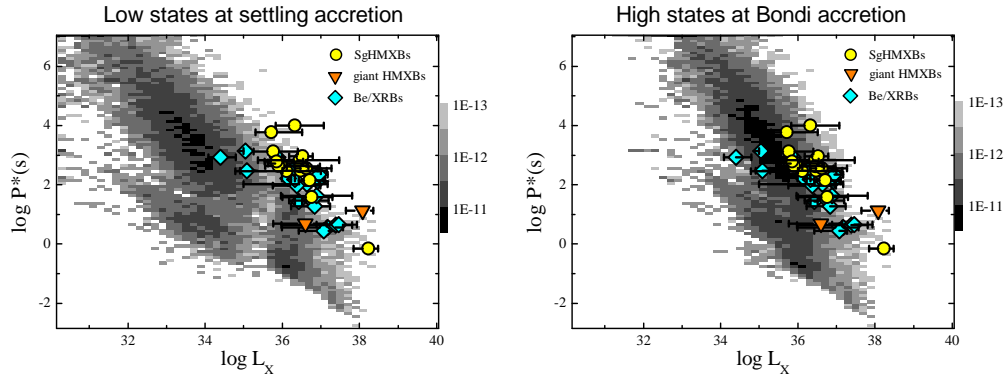


Figure 3. Model $P^* - L_x$ distribution of HMXBs (in grey scale, normalized to one M_\odot of the Galactic mass) and observed persistent HMXBs (filled circles). Filled diamonds show BeXRBs with non-circular orbits in outbursts.

disc in the form suggested by Yu & Jeffery (2010):

$$\frac{\text{SFR}(t)}{M_\odot \text{ yr}^{-1}} = \begin{cases} 11e^{-\frac{t-t_0}{\tau}} + 0.12(t-t_0) & t \geq t_0, \\ 0 & t < t_0 \end{cases} \quad (4.1)$$

with time t in Gyr, $t_0=4$ Gyr, $\tau = 9$ Gyr. Assumed Galactic age is 14 Gyr. This model gives total mass of Galactic bulge and thin disk $M_G = 7.2 \times 10^{10} M_\odot$, which we will use for normalization of our calculation results.

To illustrate the effect of different regimes of wind accretion in HMXBs, in Fig. 3 we show in grey scale the model Galactic distribution of equilibrium periods P^* of NSs in HMXBs vs. their X-ray luminosity L_x normalized to one M_\odot . The range of observed L_x of persistent wind-accreting HMXBs is taken from Sidoli & Paizis (2018). Outburst X-ray luminosity of BeXRBs with eccentric orbits are shown by filled blue diamonds. As discussed above, a wind-accreting NS can reach long spin periods at the subsonic settling accretion stage. However, when the accretion X-ray luminosity exceeds $\sim 4 \times 10^{16}$ [erg s $^{-1}$], the supersonic Bondi accretion regime sets in, at which the NS acquires angular momentum from captured wind matter. Therefore, we plot separately the model $P^* - L_x$ distribution for the settling accretion regime (left panel in Fig. 3) and the Bondi X-ray luminosity for the same sources ($L_{x,B} = 0.1 M_B c^2$) (right panel in Fig. 3). Clearly, the observed location of persistent HMXBs and BeXRBs on this diagram better corresponds to the Bondi accretion luminosity (but see the discussion of Vela X-1 and GX 301-2 in (Shakura et al. 2012)), and the model left and right panels show the expected X-ray luminosity range between settling and Bondi accretion stages. The actual situation may be due to a selection effect: the brightest sources correspond to the more luminous Bondi accretion, and a bulk of possible dimmer sources with about solar X-ray luminosity are yet to be identified in more sensitive observations.

In Fig. 4 we plot the calculated distribution of sources in the X-ray luminosity – orbital period plane. Like in Fig. 3, the left and right panels correspond to settling and Bondi accretion states, respectively. The model $P^* - P_b$ distribution (the Corbet diagram) for wind accreting HMXBs is shown in the left panel of Fig. 5. Separately, in the right panel of Fig. 5, model HMXBs with supercritical Shakura-Sunyaev accretion discs are shown (in grey scale). Observed pulsating ULXs with known orbital periods (Bachetti et al. 2014; Fürst et al. 2016; Israel et al. 2017a,b) are shown by red open circles. In Fig. 6 we plot the model distribution of HMXBs with neutron stars with supercritical accretion discs

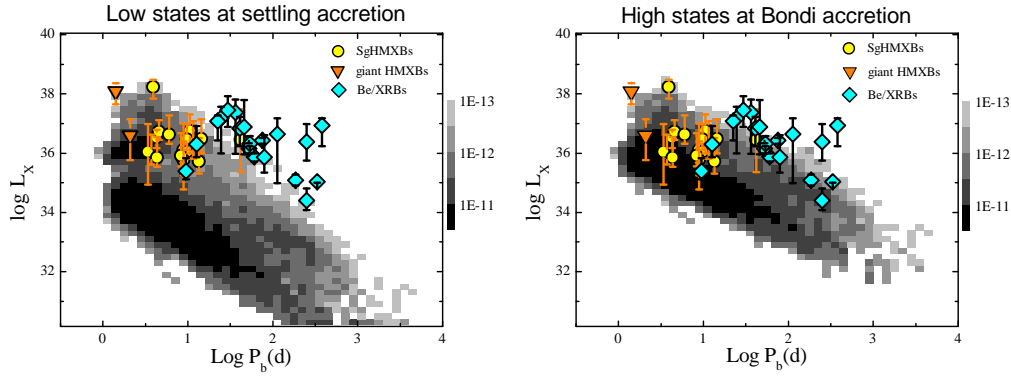


Figure 4. Model X-ray luminosity L_x – binary orbital period diagram for HMXBs (in grey scale) and observed steady sources (filled circles). Filled diamonds show BeXRBS with non-circular orbits in outbursts. Data from Sidoli & Paizis (2018).

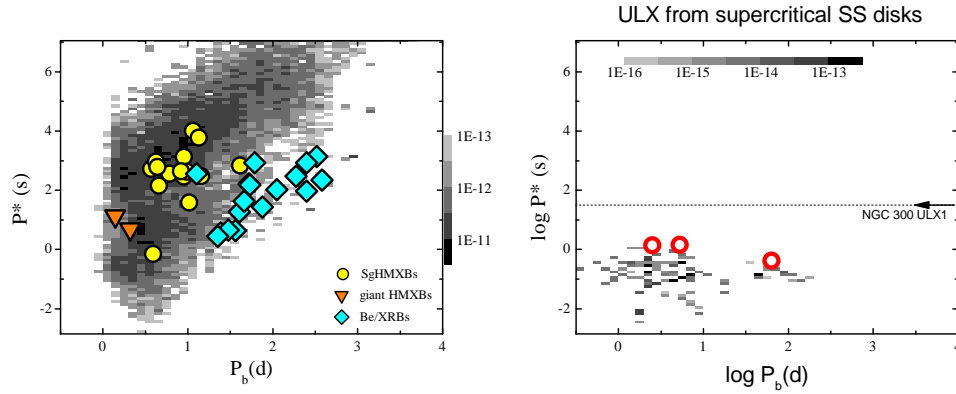


Figure 5. Left: model NS spin period P^* – binary orbital period P_b diagram (the Corbet diagram) for HMXBs (in grey scale) and observed steady sources (filled circles). Filled diamonds show BeXRBS with non-circular orbits. Data from Sidoli & Paizis (2018). Right: the Corbet diagram for NSs at supercritical accretion disc stage. Open red circles show pulsating ULXs, dashed line indicates P^* of NGC 300 ULX1.

and observed pulsating ULXs (red open circles). In addition to the observed pulsating ULXs shown in the Corbet diagram (right panel of Fig. 5), we plot there also candidate ULX NGC 300 ULX1 with $P^* \simeq 31.7$ s, $L_x \simeq 4.7 \times 10^{39}$ [erg s $^{-1}$] (Carpano et al. 2018).

5. Discussion and conclusions

In wind accreting HMXBs with magnetized NSs, two regimes of accretion should be distinguished: the supersonic Bondi-Hoyle-Littleton accretion at high accretion rates, $\dot{M} \gtrsim 4 \times 10^{16}$ [g s $^{-1}$] (high X-ray luminosity $L_x > 4 \times 10^{36}$ [erg s $^{-1}$]) and subsonic settling accretion (lower L_x). In the regime of settling accretion, a hot shell is formed around the NS magnetosphere enabling angular momentum transfer to/from the rotating NS, and NS reaches an equilibrium spin period proportional to the orbital binary period P_b . Only spin-up of NS is possible in the Bondi-Hoyle accretion stage.

The Corbet diagram for HMXBs. We performed population synthesis calculations of HMXBs with magnetized NSs under standard assumptions on the massive binary star

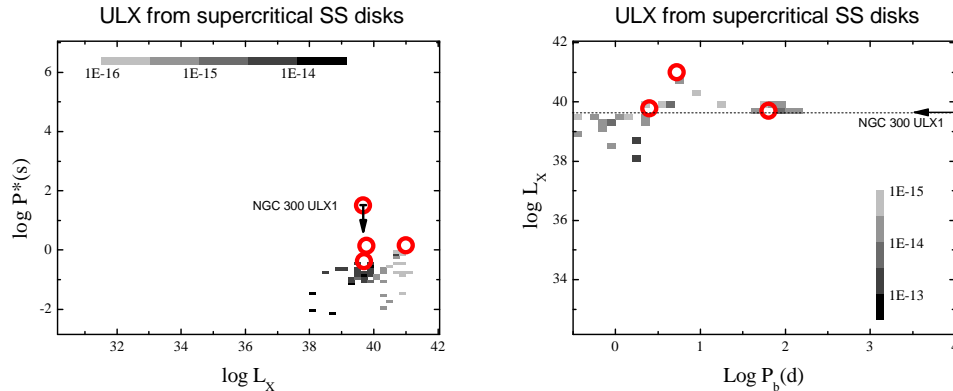


Figure 6. Model $P^* - L_x$ and $L_x - P_b$ diagrams (left and right panels, respectively) for NSs in HMXBs at supercritical accretion disc stage (in grey color, normalized to one M_\odot of Galactic mass). Open red circles show pulsating ULX. NGC 300 ULX X-1 is marked with black arrow.

evolution, parameters of stellar wind for early type massive stars and magnetic fields of NSs as inferred from radio pulsars observations.

Inspection of model distribution $P^* - L_x$ (Fig. 3) suggests that NSs in wind-accreting HMXBs have reached the equilibrium spin period at the early settling accretion stage, but the observed X-ray luminosities better correspond to the Bondi-Hoyle mass accretion rate from the stellar wind (right panel of Fig. 3). The latter holds true for the model $L_x - P_b$ distribution of HMXBs (Fig. 4): the Bondi-Hoyle accretion rates better correspond to observations (right panel of Fig. 4), suggesting earlier stage of settling accretion at which NSs have reached the equilibrium spin periods. This conclusion is supported by the model $P^* - P_b$ distribution of HMXBs (the Corbet diagram) shown in Fig. 5, left panel. Parameters of the observed quasi-steady HMXBs (filled yellow circles and triangles) are in good agreement with the model. However, the observed Be X-ray binaries shown by filled blue diamonds are located systematically lower in this diagram, most likely, due to the reduction of the equilibrium spin period due to orbital eccentricity by the factor $F(e)$ (see Eq. (2.7)) presented in Fig. 1.

The Corbet diagram for pulsating ULXs. When a massive optical star in HMXB overfills its Roche lobe, a supercritical accretion disc can be formed around a magnetized NS. Then the formulas shown in Fig. 2 should be used to calculate the NS equilibrium spin period P^* and X-ray luminosity L_x (in the case where \dot{M} in the disc exceeds \dot{M}_{cr} defined in Sec. 3). Population synthesis calculations of the HMXBs that during later evolution produced objects hosting supercritical accretion discs shown in Fig. 5, right panel (the Corbet diagram for ULXs) and Fig. 6 suggest that pulsating ULXs with known spin P^* and orbital periods P_b fall almost precisely into the expected distribution (shown in grey scale normalized to one M_\odot of the Galactic mass). We stress that in these calculations, we have not done any special assumptions about NS properties (e.g., the initial magnetic field distribution, which is assumed to be a Gaussian centered at 10^{12} G) or binary stellar evolution, i.e. the wind-accreting HMXBs and pulsating ULXs represent single evolutionary related population. Here we stress that the equilibrium NS spin periods and luminosities at supercritical accretion stages depend only on the NS magnetic field (see formulas in Fig. 2). Therefore, the observed dispersion in spin periods of pulsating ULXs around ~ 1 sec reflects the dispersion of magnetic fields of superaccreting NSs in HMXBs. It is clear that to explain these spin periods, no hypothesis of unusual magnetic fields of NSs is needed.

The 31.7-s NGC 300 ULX1 shown as the upper circle in the left panel of Fig. 6, is worth special mentioning. Its record-high observed spin-up rate (Carpano et al. 2018) $\dot{P} \sim 5 \times 10^{-7} [\text{s s}^{-1}]$ suggests a NS spinning-up towards equilibrium. Our model presented in Fig. 2 immediately implies that for $\dot{M} > \dot{M}_{cr}$ (which is the case for the observed X-ray luminosity $\sim 5 \times 10^{39} [\text{erg s}^{-1}]$), the spin-up rate far from equilibrium is $\dot{P} = P^2 / (2\pi I) \sqrt{GM_x R_A} \approx P^2 / (2\pi I) \sqrt{GM_x \times 6.5 \cdot 10^7 (L_x / (65 L_{Edd}))} \simeq 5 \times 10^{-7} [\text{s s}^{-1}]$, in perfect agreement with observations.

Acknowledgements. KP acknowledges grant RSF 16-12-10519 for partial support (Section 1-3). The work of AK (Section 4) is supported by RSF grant No. 14-12-00146.

References

- Arons, J. & Lea, S.M. 1976, *ApJ*, 207, 914
Arons, J. & Lea, S.M. 1980, *ApJ*, 235, 1016
Bachetti, M. et al. 2014, *Nature*, 514, 202
Burnard, D.J., Arons, J., & Lea, S.M. 1983, *ApJ*, 266, 175
Carpano, S., Haberl, F., Maitra, C., & Vasilopoulos, G. 2018, *MNRAS*, 476, L45
Chakrabarty, D. et al. 1997, *ApJL*, 481, L101
de Val-Borro, M., Karovska, M., Sasselov, D.D., & Stone, J.M. 2017, *MNRAS*, 468, 3408
Fürst, F. et al. 2016, *ApJL*, 831, L14
González-Galán, A. et al. 2012, *A&A*, 537, A66
Ho, C., Taam, R.E., Fryxell, B.A., Matsuda, T., & Koide, H. 1989, *MNRAS*, 238, 1447
Hunt, R. 1971, *MNRAS*, 154, 141
Hurley, J.R., Pols, O.R., & Tout, C.A. 2000, *MNRAS*, 315, 543
Hurley, J.R., Tout, C.A., & Pols, O.R. 2002, *MNRAS*, 329, 897
Illarionov, A.F. & Sunyaev, R.A. 1975, *A&A*, 39, 185
Israel, G.L. et al. 2017a, *Science*, 355, 817
Israel, G.L. et al. 2017b, *MNRAS*, 466, L48
King, A., Lasota, J.P., & Kluźniak, W. 2017, *MNRAS*, 468, L59
Knigge, C., Coe, M.J., & Podsiadlowski, P. 2011, *Nature*, 479, 372
Lipunov, V.M. 1982, *SvA Lett.*, 26, 54
Lipunov, V.M., Postnov, K.A., Prokhorov, M.E., & Bogomazov, A.I. 2009, *Astronomy Reports*, 53, 915
Liu, Z.W., Stancliffe, R.J., Abate, C., & Matrozi, E. 2017, *ApJ*, 846, 117
Lü, G.L. et al. 2012, *MNRAS*, 424, 2265
Postnov, K.A. & Yungelson, L.R. 2014, *Living Reviews in Relativity*, 17, 3
Shakura, N. & Postnov, K. 2017, *ArXiv e-prints*
Shakura, N., Postnov, K., Kochetkova, A., & Hjalmarsdotter, L. 2012, *MNRAS*, 420, 216
Shakura, N., Postnov, K., Kochetkova, A., & Hjalmarsdotter, L. 2018, in: N. Shakura, ed., *Accretion Processes in Astrophysics*, chap. 8, Springer:
Shakura, N.I. & Sunyaev, R.A. 1973, *A&A*, 24, 337
Sidoli, L. & Paizis, A. 2018, *MNRAS*, 481, 2779
Vink, J.S. 2018, *ArXiv e-prints*, 1808.06612
Yu, S. & Jeffery, C.S. 2010, *A&A*, 521, A85